Electronic Supplementary Material (ESI) for CrystEngComm.

Controllable synthesis of NiCo layered double hydroxide sheets on laser induced graphene as electrodes for high performance supercapacitor

Xinru Xing, Zijie Qu, Lei Ge, Xinzhi Sun*, Feng Li

College of Chemistry and Pharmaceutical Sciences, Qingdao Agricultural University, ChangCheng Road 700, Chengyang, Qingdao 266109, People's Republic of China

*Corresponding author

E-mail: xzsun@qau.edu.cn (X. Sun)

Materials and reagents. Kapton polyimide (PI) sheet (500HN, thickness: 125 μm) were supplied by DuPont. All other reagents were of analytical grade and used without further purification.

2. Experimental sections

2.1 Preparation of laser-induced graphene (LIG)

Laser scribing on PI films were conducted using a CO_2 laser (10.6 μm wavelength) cutter system (Universal X-660 laser cutter platform). The total laser power was 40 W and the laser system provides an option of setting a laser power. The laser power was set as 10%, 12% and 14% of the full power, which was 4 W, 4.8 W and 5.6 W, respectively. The scan speed and laser dots per inch (DPI) were set to 7.2 mm s^{-1} and 1200, respectively. In the process of scribing, automatic focus is used to reduce the error of laser Z-distance measurement. All experiments were carried out at normal temperature and ambient air.

The laser-induced graphene was scribed from the PI film and graphene powders were obtained

2.2 Preparation of the working electrode

Commercial active carbon (AC) was used as the negative electrode and NiCo-LDH@PX-LIG was employed as the positive electrode material.

The positive electrode consisted of NiCo-LDH@PX-LIG, with a mass ratio of 8:1:1, acetylene black and polyvinylidene fluoride (PVDF), which was ground and mixed well. Subsequently, the mixed powders were mixed with a drop of 1-Methyl-2-Pyrrolidone and continuously grinding till a homogeneous slurry was obtained. Finally, the slurry was applied on a nickel foam (painted area of 1 cm^2), further pressed at 10 MPa for 60 s and then dried at 80 ℃ overnight. The preparation process of the negative electrode was the same as that of the positive electrode except that NiCo-LDH@PX-LIG was used instead of commercial AC.

In order to obtain the best electrochemical performance of the two electrodes, the relationship between the masses of the negative and positive electrodes is expressed by the following equation [1-3].

$$\frac{m_+}{m_-} = \frac{C_- \cdot \Delta V_-}{C_+ \cdot \Delta V_+}$$

Where m_+, m_-, C_+, and C_- are the mass and the specific capacitance of NiCo-LDH@PX-LIG and AC electrodes, respectively. ΔV_- and ΔV_+ are the voltage window of the negative and positive electrodes, respectively. The calculated AC masses in the five electrodes range is between 10 mg cm^{-2} and 15 mg cm^{-2}.

2.3 Materials characterization.

The surface morphology of all samples was observed by field-emission scanning electron microscopy (FESEM, Hitachi, Japan, JEOL-7500F) operated at 10 kV. The average thickness of the as-prepared products was calculated by the cross-section SEM. The structure of all samples was evaluated on a Philips X'pert diffractometer (Rigaku D/MAX-2500/PC) equipped with Cu *K* radiation (λ= 1.5418 Å). The 2θ range was setting from 5° to 60° at a scan rate of 0.5 min^{-1}. Transmission electron microscopy (TEM) images were measured on a Tecnai G2-F30 with an accelerating voltage of 300 kV and the detailed morphology of inside the materials was got. The selected area electron diffraction (SAED) was well gained by HRTEM. BET surface area and pore size distribution were evaluated by N_2 adsorption–desorption isotherms measured on an N_2 adsorption/desorption analyzer (ASAP 2420, Micrometrics, USA). Raman spectra were measured by using a Raman microscope system (DXR2xi, Thermo Fisher Scientific, Inc., USA) with an excitation line of 532 nm.

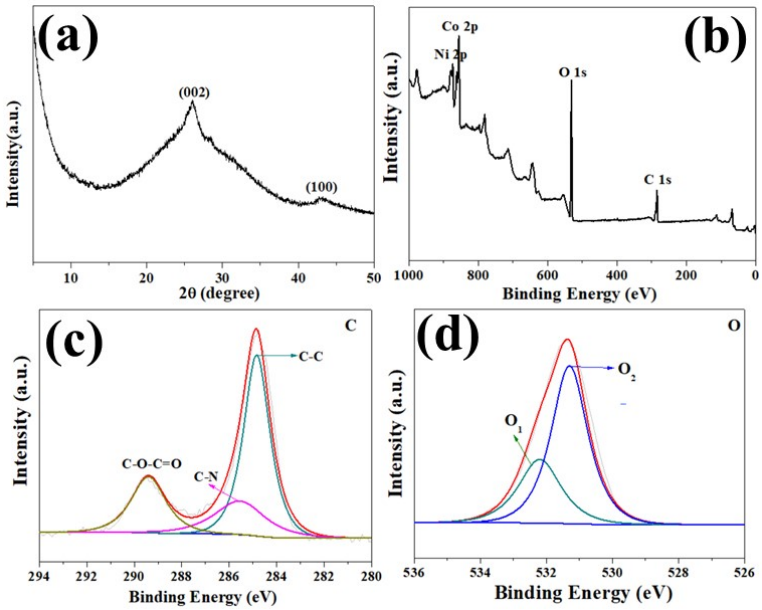

Fig. S1 (a) XRD pattern of LIG, (b) XPS survey spectrum of LIG/Ni-Co LDH, the high-resolution XPS spectra of (c) C 1s and (d) O 1s

Table S1 the content of different elements in the NiCo-LDH@PX-LIG

Element	Wt%
C	5.63
O	32.27
Co	14.28
Ni	47.83
Total:	100.00

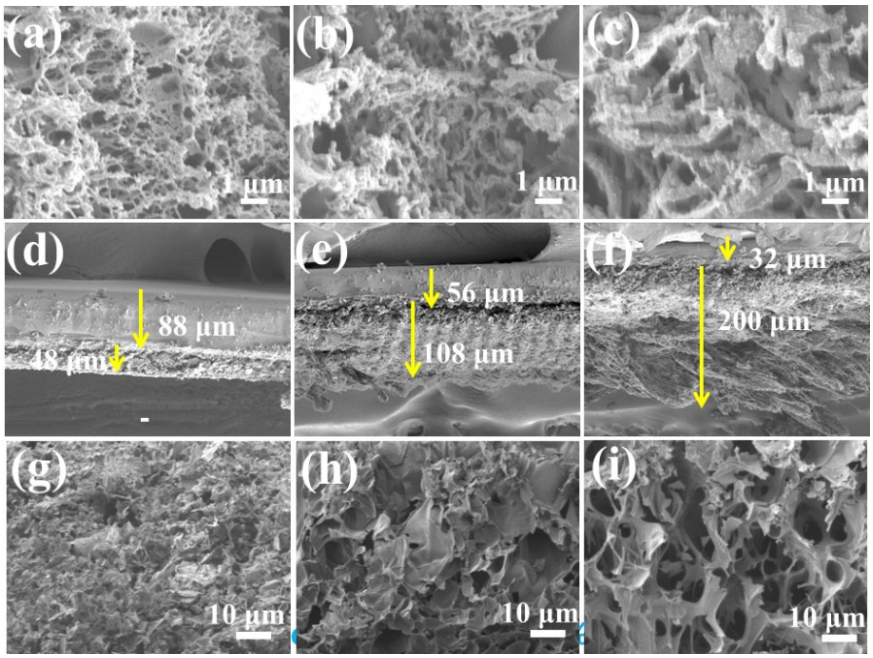

Fig. S2 Top-view SEM images of LIG induced under different laser powers (a) P10-4 W, (b) P12-4.8 W, (c) P14-5.6 W; Cross-sectional SEM images of LIG scribed under different laser powers (d) P10-4 W, (e) P12-4.8 W, (f) P14-5.6 W, high modification of cross-sectional SEM images showing the porous morphology of LIG, (g) P10-4 W, (h) P12-4.8 W, (i) P14-5.6 W

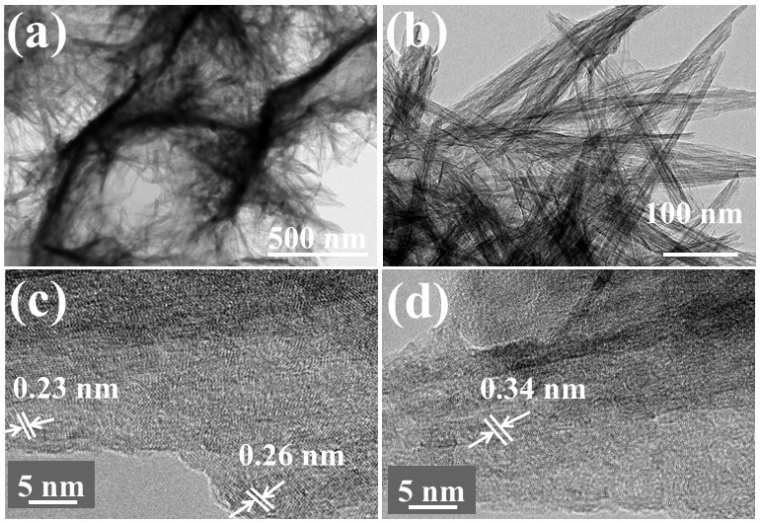

Fig. S3 SEM images of LIG-P10/Ni-Co LDH (a) and (b) at lower and higher modifications, HRTEM images of LIG-P10/Ni-Co LDH (c) (d)

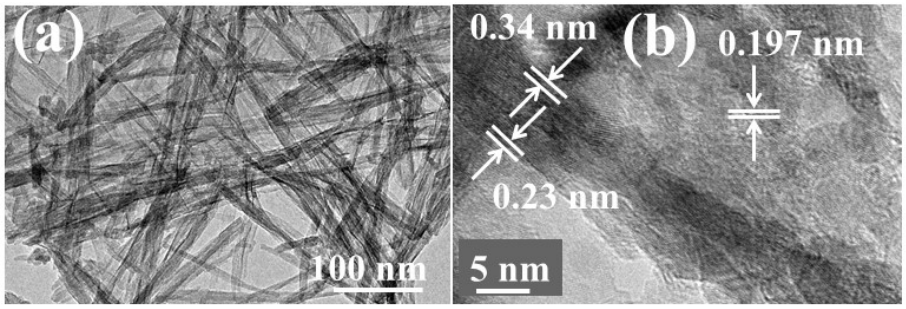

Fig. S4 TEM images of LIG-P14/Ni-Co LDH (a) and (b) HRTEM images of LIG-P14/Ni-Co LDH

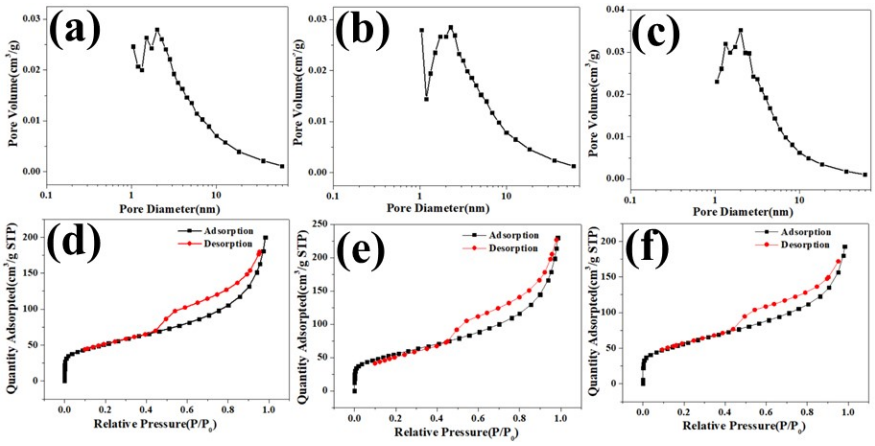

Fig. S5 The pore size distribution of the NiCo-LDH@P10-LIG (a), NiCo-LDH@P12-LIG (b) and NiCo-LDH@P14-LIG (c), and N_2 adsorption-desorption curves of the NiCo-LDH@P10-LIG (d), NiCo-LDH@P12-LIG (e) and NiCo-LDH@P14-LIG (f)

Table S2 The pore parameters of the samples

	NiCo-LDH@P10-LIG	NiCo-LDH@P12-LIG	NiCo-LDH@P14-LIG
BET (m^2 g^{-2})	182.32	196.58	201.48
Average pore diameter (nm)	6.79	7.23	5.9
Total pore volume (cm^3 g^{-1})	0.31	0.35	0.29
Volume in nanopores (%)	33	30	35
Volume in mesopores (%)	67	70	65
Volume in macropores (%)	0.33	0.35	0.25

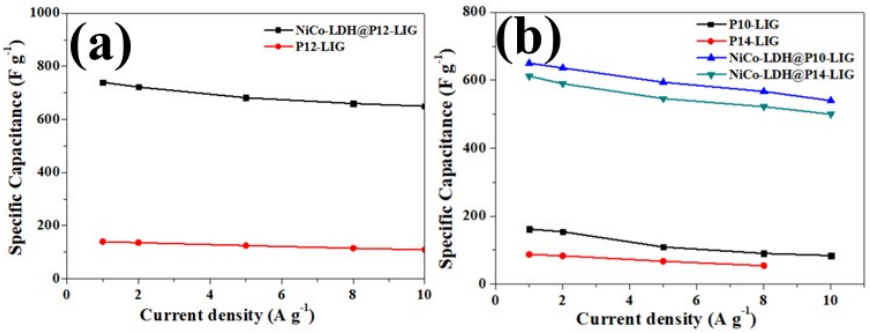

Fig. S6 The gravimetric capacitance of P12-LIG and NiCo-LDH@P12-LIG at various current densities (a), the gravimetric capacitance of P10-LIG, P14-LIG, NiCo-LDH@P10-LIG and NiCo-LDH@P14-LIG at various current densities,

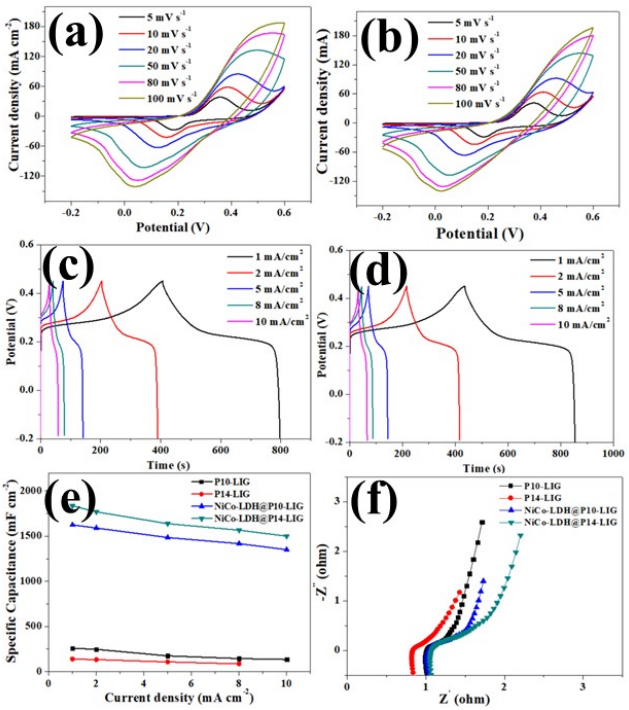

Fig. S7 CV curves of NiCo-LDH@P10-LIG (a) and NiCo-LDH@P14-LIG (b) at the various scan rates, GCD curves of NiCo-LDH@P10-LIG (c) and NiCo-LDH@P14-LIG (d) at the different current densities, (e) Areal capacitance of P10-LIG, P14-LIG, NiCo-LDH@P10-LIG and NiCo-LDH@P14-LIG at various current densities, (f) Nyquist plots P10-LIG, P14-LIG, NiCo-LDH@P10-LIG and NiCo-LDH@P14-LIG

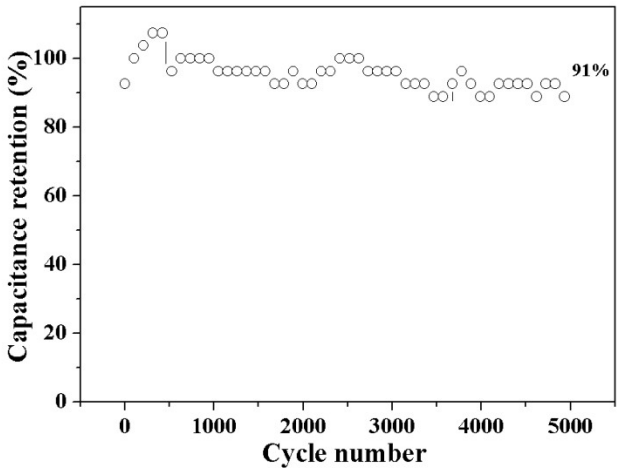

Fig. S8 Cylic stability of the NiCo-LDH@P12-LIG electrode material at 100 mA cm^{-2} for 5000 cycles

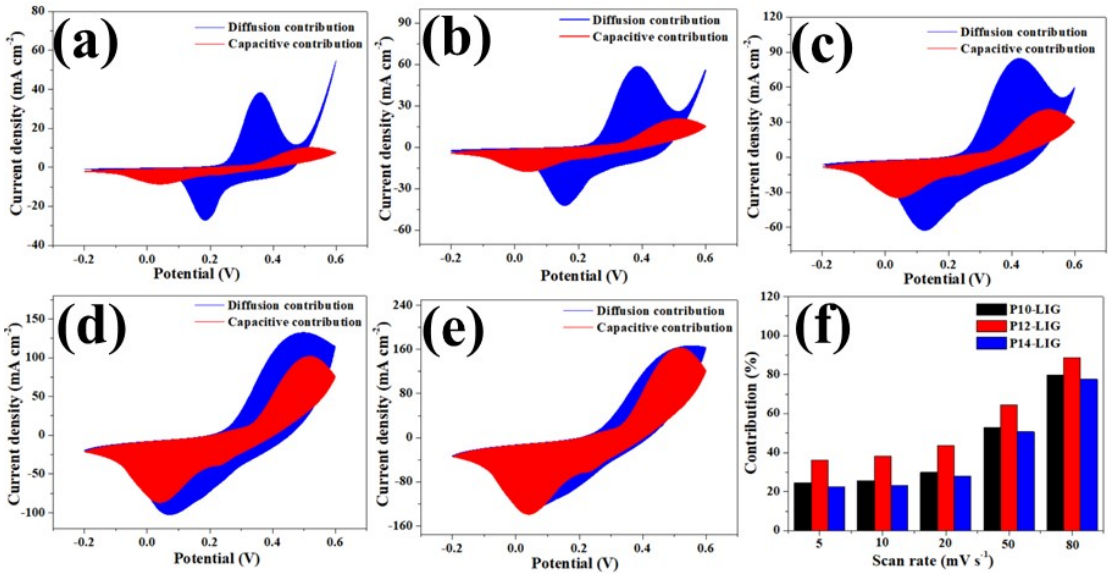

Fig. S9 The analysis of ion diffusion and capacitive contributions of NiCo-LDH@P12-LIG at different scan rate (a) 5 mV s^{-1}, (b) 10 mV s^{-1}, (c) 20 mV s^{-1}, (d) 50 mV s^{-1}, (e) 80 mV s^{-1}, (f) the normalized contribution of as-prepared samples at different scan rates

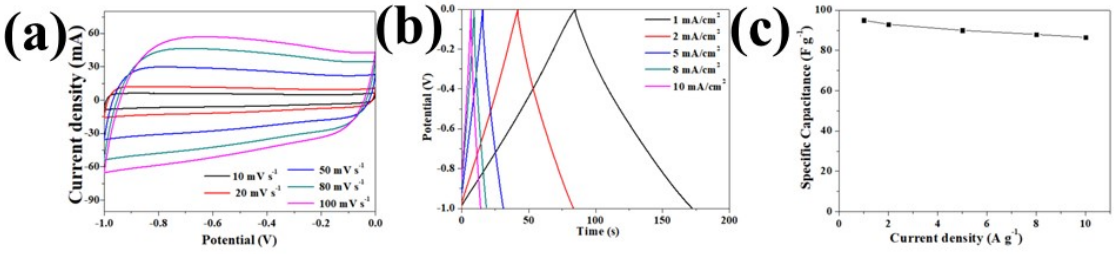

Fig. S10 CV curves (a), GCD curves (b) at various scan rates and different current densities of AC and specific capacitance at different current density (c)

Table S3 Comparison of the cycling stability of NiCo-LDH@P12-LIG electrode with some reported results

Electrode materials	Cycles	Capacitance retention	Ref.
$Ni(OH)_2$/ $Co(OH)_2$/GO	1000	84%	[4]
rGO	5000	84%	[5]
GO/PANI/ $Ni(OH)_2$	2000	84.4%	[6]
NiCo-LDH/CFC	5000	82%	[7]
NixCoy(OH)/RGO	3000	75%	[8]
$NiCo_2S_4$/Ni-Co-OH	2000	56%	[9]
NiCo-LDH@P12-LIG	6000	92%	This work

Table S4 Comparison of electrochemical performances of various LIG-based ASCs

Electrode	Current density (mA cm^{-2})	Areal capacitance (mF cm^{-2})	Ref.
NB1-dLIG-SC	0.05	40.4	[10]
LIG-FeOOH// LIG-MnO_2	0.25	21.9	[11]
L-P LIG-P15	0.5	22	[12]
5B-LIG	0.05	16.5	[13]
LSG-P24	0.05	25.1	[14]
Laser-induced MOF-derived graphene	0.15	1.36	[15]
KOH-activated graphene in-plane MSCs	0.05	32	[16]
NiCo-LDH@P12-LIG//AC	2.5	720	This work

References

[1] V. Khomenko, E. Raymundo-Piñero and F. Béguin, *Journal of Power Sources*, 2006, **153**, 183-190.

[2] Y. Jiang, C. Tang, H. Zhang, T. Shen, C. Zhang and S. Liu, *Journal of Materials Chemistry A*, 2017, **5**, 5781-5790.

[3] K. Krishnamoorthy, P. Pazhamalai, S. Sahoo, J. H. Lim, K. H. Choi and S. J. Kim, *ChemElectroChem*, 2017, **4**, 3302-3308.

[4] X. Lei, Z. Shi, X. Wang, T. Wang, J. Ai, P. Shi, R. Xue, H. Guo and W. Yang, *Colloids and Surfaces A: Physicochemical and Engineering Aspects*, 2018, **549**, 76-85.

[5] T. X. Tran, H. Choi, C. H. Che, J. H. Sul, I. G. Kim, S. M. Lee, J. H. Kim and J. B. In, *ACS Appl Mater Interfaces*, 2018, **10**, 39777-39784.

[6] J. Zhang, Y. Liu, H. Guan, Y. Zhao and B. Zhang, *Journal of Alloys and Compounds*, 2017, **721**, 731-740.

[7] J. Li, C. Hao, S. Zhou, C. Huang and X. Wang, *Electrochimica Acta*, 2018, **283**, 467-477.

[8] C. Xiang, Z. She, Y. Zou, J. Cheng, H. Chu, S. Qiu, H. Zhang, L. Sun and F. Xu, *Ceramics International*, 2014, **40**, 16343-16348.

[9] Y. Tang, Y. Liu, S. Yu, S. Mu, S. Xiao, Y. Zhao and F. Gao, *Journal of Power Sources*, 2014, **256**, 160-169.

[10] M. Khandelwal, C. V. Tran, J. Lee and J. B. In, *Chemical Engineering Journal*, 2022, **428**, 131119.

[11] L. Li, J. Zhang, Z. Peng, Y. Li, C. Gao, Y. Ji, R. Ye, N. D. Kim, Q. Zhong, Y. Yang, H. Fei, G. Ruan and J. M. Tour, *Advance Materials*, 2016, **28**, 838-845.

[12] X. Sun, X. Liu and F. Li, *Applied Surface Science*, 2021, **551**, 149438.

[13] R. Y. Zhiwei Peng, Jason A. Mann, Dante Zakhidov, Yilun Li, Preston R. Smalley, Jian Lin, James M. Tour, *ACS Nano*, 2015, **9**, 5868–5875.

[14] W. Zhang, Y. Lei, F. Ming, Q. Jiang, P. M. F. J. Costa and H. N. Alshareef, *Advanced Energy Materials*, 2018, **8**, 1801840.

[15] A. Basu, K. Roy, N. Sharma, S. Nandi, R. Vaidhyanathan, S. Rane, C. Rode and S. Ogale, *ACS Applied Materials & Interfaces*, 2016, **8**, 31841-31848.

[16] H. Liu, Y. Xie, J. Liu, K.-s. Moon, L. Lu, Z. Lin, W. Yuan, C. Shen, X. Zang, L. Lin, Y. Tang and C.-P. Wong, *Chemical Engineering Journal*, 2020, **393**, 124672.